Journal of Applied Polymer SCIENCE

Functionalized polymeric silver nanoparticle hybrid network as a dual antimicrobe: Synthesis, characterization, and antibacterial application

T. S. Anirudhan, Binusreejayan, J. R. Deepa

Department of Chemistry, School of Physical and Mathematical Sciences, University of Kerala, Kariavattom, Thiruvananthapuram, India-695581
Correspondence to: T. S. Anirudhan (E-mail: tsani@rediffmail.com)

ABSTRACT: The present work describes a novel method for the synthesis of silver polymer nanocomposite for the delivery of amoxicillin (AMO). Silver nanoparticles (AgNPs) were synthesized with chitosan and silver nitrate. The reaction parameters were optimized. Three-dimensional polymeric networks were synthesized by simple free-radical graft copolymerization. UV–visible spectroscopy, Fourier transform infrared spectroscopy, X-ray diffraction, SEM, atomic force microscopy, dynamic light scattering, and zeta potential analysis were used for the complete characterization of the samples. Swelling studies and swelling factors were evaluated. *In vitro* release of AMO and AgNPs at physiological pHs was analyzed using the Peppas kinetic model to explain the drug delivery mechanism. Cytotoxicity, free-radical scavenging, and antibacterial activities were analyzed. © 2016 Wiley Periodicals, Inc. J. Appl. Polym. Sci. **2016**, *133*, 43479.

INTRODUCTION

Nowadays human beings are at high risk of infections from their living environments by microorganisms such as bacteria, molds, and yeasts.[1,2] Thus, the scientific community gives much attention to the discovery of new and cost-effective antimicrobial agents.[3] But wide use of these agents leads to antibiotic resistance, which in turn becomes a serious issue for human health.[4] Altering the structure of bacteria and using dual-action antimicrobes are the most common techniques applied to overcome bacterial resistance. Dual-action antimicrobes have two antibiotics: one of them will be active against infections, though the other is resisted by bacteria.[5–8]

Inorganic nanomaterials have excellent antimicrobial properties.[4] Recent developments in the field of nanotechnology provide advanced methods to overcome bacterial resistance by using inorganic nanoparticles. Silver (0) nanoparticles (AgNPs) are the most powerful, long-known antimicrobial agent.[9] AgNPs have a variety of physical, chemical, and biological properties, along with polyvalent binding capacity, chemical stability, and unique particle size.[10] A large number of reports are available for the synthesis of AgNPs by various physical,[11–13] chemical,[14–16] and biological[17] methods. The physical methods involve the use of gamma rays, microwave radiation, and so on, and in biological methods microorganisms are applied. In chemical methods, reducing agents are utilized in the presence of stabilizing agents. The physical reduction methods

are quite expensive, and conventional chemical reducing agents show certain toxicological effects.[18]

The application of green chemistry principles to the synthesis of metallic nanoparticles by using polysaccharides, oligosaccharides, and so on are found to be the highly cost-effective, eco-friendly, and greener method.[18,19] AgNPs coated with polysaccharide can easily bind with the living cell surface and improve intracellular uptake and biocompatibility.[20]

Among various natural polysaccharides, chitosan (CT) and its derivatives are well known for their excellent antimicrobial and antifungal activity[21–23] because of their inherent ability to bind with DNA and proteins present on the cell walls of bacteria.[24] Antibacterial activity of CT persists only in an acidic medium because of its low solubility at pHs above 6.5.[25] CT is the second most abundant nontoxic cationic polysaccharide, composed of β-(1,4)−2-amino-2-deoxy-*D*-glucose and is widely used in the biomedical field because of its excellent physiochemical properties and its biocompatibility and biodegradability in an aqueous environment.[26–29] Our research group has already reported the use of a thiolated chitosan/poly(lactic acid) blend incorporated in methionine-modified montmorillonite for the controlled release of amoxicillin (AMO) in the intestinal pH.[30]

The hydrophilic nature and higher solubility of CT in an acidic medium prevents its ability to control the release of drug

molecules. Hence, chemical modification to the primary hydroxyl or amino groups present on CT is a necessity.[31] Graft copolymerization of vinyl monomers on the CT chain results in a polymer tailored with the desired functionalities that can improve or impart the required physical properties of a typical drug carrier. The production and application of hydrogels containing metallic nanoparticles for biomedical applications are still moving forward.[32] The novel materials have the hybrid qualities of both polymers and nanoparticles, but for biomedical applications they should have low toxicity, cost effectiveness, and easy synthesis.

AgNPs embedded in a hydrogel network are a necessity in improving the release time of silver and the antimicrobial activity and reducing the agglomeration of synthesized nanoparticles.[33] Nanoparticle hydrogels can be synthesized by three different mechanisms: (1) a breathing mechanism, in which nanoparticles in solution are moved into a hydrogel during swelling, (2) fabrication of the nanoparticles inside a hydrogel by an *in situ* process, and (3) copolymerization of monomers and surface-modified nanoparticles.[34]

Films,[35] beads,[36] and composites[37] from CT-based AgNPs as antimicrobial and drug delivery systems have already been reported. Most of them reported the synthesis of AgNPs by making use of toxic chemicals as reducing agents. But the use of functionalities present on CT in the composite for the synthesis of a hydrogel or the combined effect of AMO with CT-based AgNPs is not yet reported.

The main aim of the present study is to synthesize AgNPs with CT, an ecofriendly reducing and nontoxic capping agent. Itaconic acid (IA) is grafted onto CT, coated on the surface of AgNPs, using ceric ammonium nitrate (CAN) as initiator and *N,N'*-methylenebisacrylamide (MBA) as crosslinker. This novel polymer-AgNP can act as a carrier for AMO, a β-lactam semisynthetic antibiotic with high pH sensitivity. AMO is an α-amino-hydroxybenzylpenicillin and is effective in treating intestinal bacterial infections. This single antibiotic is not effective in treating infections because of its low stability at acidic pH. Controlled delivery of AMO into the intestinal area using pH-responsive hydrogels serves to protect the drug in the gastric pH and reduce the side effects.[38–41] Thus the proposed AMO-loaded suitably designed antibacterial-active AgNP/polymer hybrid network can act as a dual antimicrobe.

EXPERIMENTAL

Materials
AMO, AgNO$_3$, CT, fetal bovine serum (FBS), 3-(4,5-dimethylthiazol-2-yl)$-$2,5-diphenyl tetrazolium bromide (MTT), ascorbic acid, and 1,1-diphenyl-2-picryl hydrazyl (DPPH) were purchased from Sigma-Aldrich, Milwaukee, WI. IA, MBA, and CAN were procured from E-Merck (Worli, Mumbai, India). L929 fibroblastic cell lines were purchased from NCCS, Pune, India. Trypsin in ethylene diamine tetraacetic acid (EDTA) solution and Dulbecco's Modified Eagle's medium (DMEM) were obtained from HiMedia Laboratories, Mumbai, India. All chemicals were of analytical grade and used as such. Distilled water

with specific conductivity less than 1 μS/cm was used for preparing solutions throughout the study.

Synthesis of Drug Carrier (IA-g-AgNP)
Step 1. Synthesis of Silver Nanoparticles (AgNPs). About 0.1% CT was stirred with 100 mL 2.0% acetic acid solution for 30 min at room temperature. To this, the aqueous AgNO$_3$ solution (1.0 mM) was added and the pH adjusted to 4.0. The reaction mixture was incubated at 25 °C for 30 min. The colorless solution changes to yellow and finally to brown, depending on the reaction condition. The solution was centrifuged at 15,000 rpm for 15 min, and the pellets of AgNPs obtained were washed thoroughly with distilled water. In order to optimize the reaction parameters on the synthesis of AgNPs, the above experiments were carried out in different reaction conditions, such as CT concentration (0.1–0.6%), AgNO$_3$ concentration (1.0–5.0 mM), initial pH (4.0–10.0), time (30 min to 5 h), and temperature (25–55 °C). The UV–visible spectra of the solutions were used to study the effect of these parameters. The final product synthesized under optimized conditions was dried and stored in the dark for further analysis.

Step 2: Synthesis of IA-g-AgNPs. The AgNPs were further modified by graft copolymerization using IA. About 0.1 g of AgNPs was sonicated with 100 mL water for 6 h in a 250 mL three-necked stoppered bottle equipped with a reflux condenser, thermometer, and nitrogen gas inlet. The solution was heated to 50 °C, and 0.005 M CAN (initiator) was added with constant stirring ($\sim$10 min). After cooling the reaction mixture to room temperature, IA (0.1 M; monomer) and MBA (0.15 M; crosslinker) were added, and the reaction was maintained for 4 h at 60 °C to complete the reaction. The obtained product was filtered, washed with distilled water to remove homopolymer, and dried. The final IA-g-AgNPs was ground and stored in a desiccator.

Characterization
Fourier transform infrared (FTIR) spectra were recorded on a Thermo Nicolet Avatar 370 spectrophotometer (Madison, WI) in transmission mode using the KBr disk technique over the spectral range from 4000 to 400 cm^{-1}. X-ray diffraction (XRD) measurements were carried out using a Bruker AXS D8 Advance (Massachusetts, US). The morphological variation was studied using a JEOL Model JSM 6390LV (Boston, USA) scanning electron microscope (SEM). Atomic force micrographs (AFM) were taken by using a Bruker DIMENSION edge with SCAN ASYST instrument. Particle size measurements were carried out using a Zetasizer Nano ZSP instrument from Malvern Instruments Ltd (Malvern, UK). The optical absorption spectrum of synthesized nanoparticles and AMO was recorded with a JASCO V-530 UV–visible spectrophotometer (Easton, MD). An atomic absorption spectrophotometer (AAS; GBC Avanta, Hampshire, IL, USA) was used to determine the concentration of AgNPs.

Estimation of Carboxyl Groups. The amount of carboxyl groups present in IA-g-AgNPs was determined by the Boehm titration method.[24] About 0.15 g IA-g-AgNPs was shaken with NaHCO$_3$ (30 mL, 0.1 M) for 20 h at room temperature and filtered. To 10 mL of filtrate, excess 0.05 M HCl was added and boiled off CO$_2$. The solution was cooled and back-titrated with

NaOH (0.05 M). The amount of carboxyl group was calculated using the equation

$$\text{COOH} \left(\frac{\text{meq}}{\text{g}}\right) = \frac{(C_{\text{NaOH}} \times V_{\text{NaOH}} - C_{\text{HCl}} \times V_{\text{HCl}})}{W} \quad (1)$$

where C and V are the concentration (M) and volume (mL) of NaOH and HCl solution used, and W is the weight of IA-g-AgNPs (g).

Swelling Studies. In order to ensure equilibrium swelling, a weighed amount of sample (0.1 g) was taken in a previously weighed tea bag and allowed to swell in the solution of desired pH (1.0–10.0) at predetermined time intervals and temperature. The swollen samples were taken out, and excess liquid droplets on the surface were removed by wiping with a tissue paper. The weights of swollen samples (W_s) were measured on an electronic balance. The swollen samples were then allowed to dry in an air oven until there was no weight change. Then W_d is the weight of the dry sample. The equilibrium swelling percentage was calculated using the equation

$$Q_{eq} = \frac{W_s - W_d}{W_d} \times 100 \quad (2)$$

The effects of electrolytes and their concentration on the swelling of IA-g-AgNPs were evaluated using NaCl, CaCl$_2$, and FeCl$_3$ salts in a buffer solution of pH 7.4 and compared with that of distilled water. The swelling factor, f, was calculated using the equation

$$f = 1 - \frac{\text{Swelling in a given fluid}}{\text{Swelling in distilled water}} \quad (3)$$

Drug Content on IA-g-AgNP. AMO-IA-g-AgNPs was prepared by mixing 50 mL AMO (2 mg/mL) with 0.1 g IA-g-AgNPs at pH 5.0 under continuous stirring for 6 h. The formed AMO-IA-g-AgNPs was separated by centrifugation (3000 rpm) and washed repeatedly with water to remove excess nonadsorbed AMO from the surface of IA-g-AgNP.

The amount of drug in the synthesized drug carrier was estimated by shaking 0.1 g of finely powdered AMO-IA-g-AgNPs in 50 mL phosphate buffer solution (pH = 7.4) for 24 h. The solution was filtered, and the amount of AMO in the filtrate was measured using a UV–visible spectrophotometer at 230 nm. A calibration curve of AMO constructed from a series of solutions with known drug concentration is used to calculate the amount of drug in the supernatant solution. The drug loading percentage (% DL) and encapsulation efficiency percentage (% EE) were calculated using the following equation:

$$\% \text{ DL} = \frac{\text{Weight of AMO in IA}-\text{g}-\text{AgNPs}}{\text{Weight of IA}-\text{g}-\text{AgNPs}} \times 100 \quad (4)$$

$$\% \text{ EE} = \frac{\text{Weight of AMO in IA}-\text{g}-\text{AgNPs}}{\text{Weight of AMO used for loading}} \times 100 \quad (5)$$

***In Vitro* Release of AMO and AgNPs.** The release behavior of AMO from IA-g-AgNPs was investigated by stirring 1.0 g of AMO-IA-g-AgNPs in 500 mL of phosphate buffer solution of pH 7.4 (simulated intestinal pH) and acetate buffer solution of pH 1.8 (simulated gastric pH). The system was maintained at

37 °C throughout the study. At regular intervals of time, 5 mL aliquots were withdrawn and filtered. The amount of AMO released into the solution was analyzed with a UV–visible spectrophotometer at $\lambda_{\max} = 230$ nm. From the calibration curve of AMO, the drug release percentage was calculated and plotted versus time using the equation

$$\text{Cumulative release (\%)} = \frac{M_t}{M_\infty} \times 100 \quad (6)$$

where M_t and M_∞ are the cumulative amount of AMO released at time t and infinite time, respectively.

To understand the release mechanism, the release data were analyzed using the Peppas kinetic equation:

$$\frac{M_t}{M_\infty} = kt^n \quad (7)$$

where k is the apparent release rate and n is the diffusion exponent.

The release of AgNPs from IA-g-AgNPs was studied by using AAS. First, 1.0 g of AMO-IA-g-AgNPs was placed in 500 mL buffer solutions of pH 7.4 and 1.8 at 37 °C. At regular time intervals, solution was withdrawn, and the concentration of AgNPs was estimated by AAS using an air/acetylene flame.[42] The percentage silver release was calculated using eq. (6) and analyzed using the Peppas equation.

Cell Viability of IA-g-AgNPs in Cultured L929 Cell Lines. The cytotoxic effect of IA-g-AgNPs was evaluated by MTT assay using L929 fibroblastic cell lines. Cells were incubated in a DMEM medium supplemented with 10% FBS at 37 °C in a humidified atmosphere with 5% CO$_2$. These cells were trypsinized (~2 min) and incubated with different concentrations (6.25, 12.5, 25.0, 50.0, and 100.0 μg/ml) of IA-g-AgNPs for 24 h. Finally, the cells were washed and stained with 50 μL MTT solution. After 4 h, the medium was discarded, and the formazan crystals were eluted with 200 μL isopropanol. The absorbance of the solution was measured at 570 nm using a microplate reader. The optical density of the control was obtained by repeating the above experiment without any sample. Viability (%) and cytotoxicity (%) were calculated using the following equation:

$$\text{Viability (\%)} = \frac{\text{Optical density of test}}{\text{Optical density of control}} \times 100 \quad (8)$$

$$\text{Cytotoxicity (\%)} = 100 - \text{viability (\%)} \quad (9)$$

Determination of Free-Radical Scavenging Activity of IA-g-AgNPs by DPPH Assay. The free-radical scavenging ability of IA-g-AgNPs was evaluated by DPPH assay. Different concentrations of the IA-g-AgNPs (1.25–20.0 μg/mL) were mixed with 0.1 mM DPPH solutions and incubated in the dark for 30 min at 37 °C. The decrease in absorbance (A) of the DPPH solutions after incubation was measured at 517 nm using a UV–visible spectrophotometer. Ascorbic acid was used as the control. The inhibition or scavenging percentage was calculated using the following equation:

$$\text{Scavenging or inhibition (\%)} = \frac{(A_{\text{control}} - A_{\text{test}})}{A_{\text{control}}} \times 100 \quad (10)$$
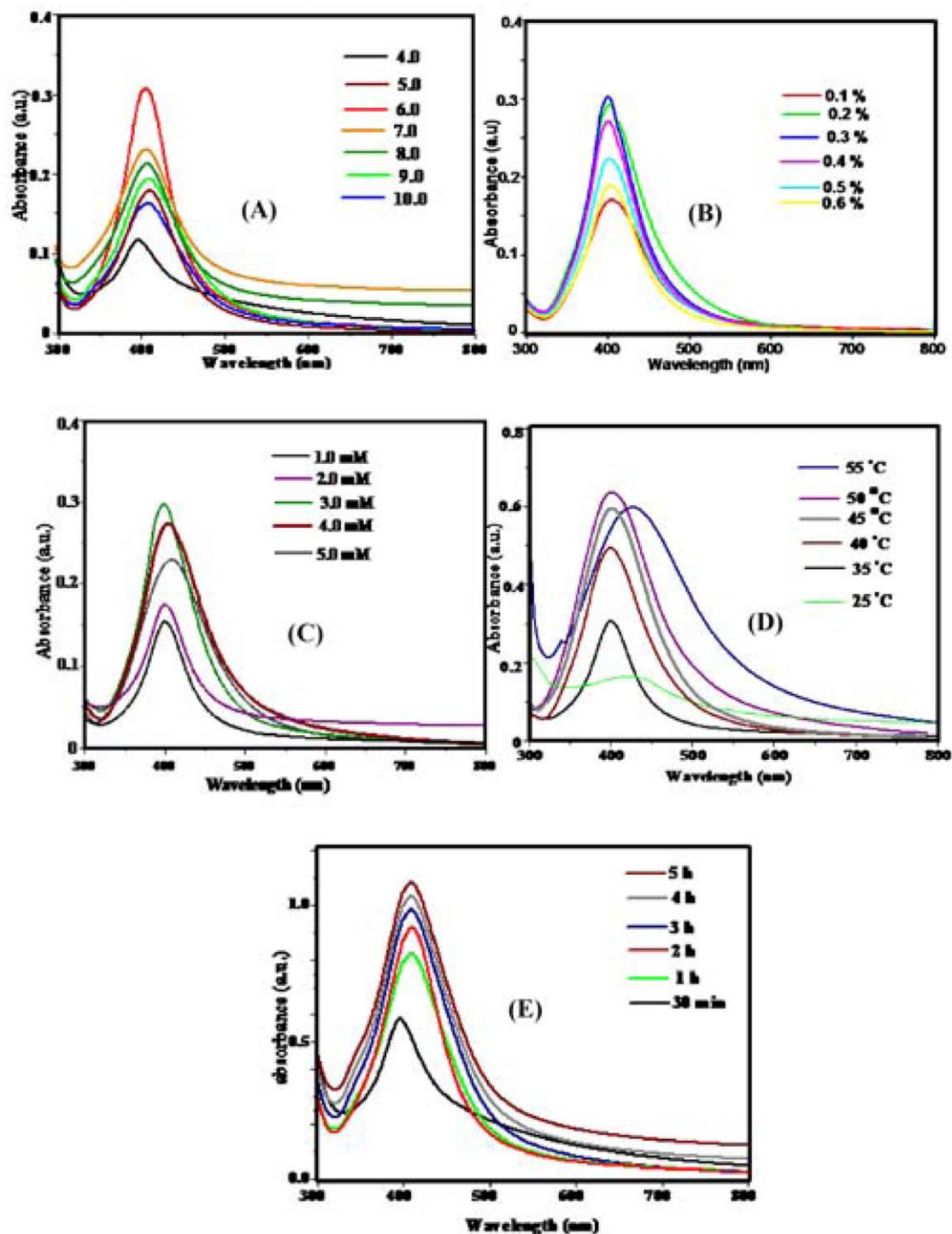
Figure 1. UV–visible spectra of the AgNPs synthesized at different (A) pH values, (B) CT concentrations, (C) $AgNO_3$ concentrations, (D) reaction temperatures, and (E) reaction times. [Color figure can be viewed in the online issue, which is available at wileyonlinelibrary.com.]

Antibacterial Assay of AMO-IA-g-AgNP. The antibacterial activity of AMO-IA-g-AgNPs was determined by using two-fold serial dilution methods. *E. coli* and *Staphylococcus* were used as the indicator organisms. First, 10.0 mg/ml of AMO-IA-g-AgNPs was dissolved in DMSO and further diluted to the desired concentrations (3.0, 6.25, 12.5, 25.0, and 50.0

µg/mL). The test pathogens were spread on agar test plates and sterile wells. Each well was loaded with the desired concentration of AMO-IA-g-AgNPs and incubated overnight. The activities of AMO-IA-g-AgNPs against bacteria were observed by measuring the zone of inhibition (mm) produced by the sample.
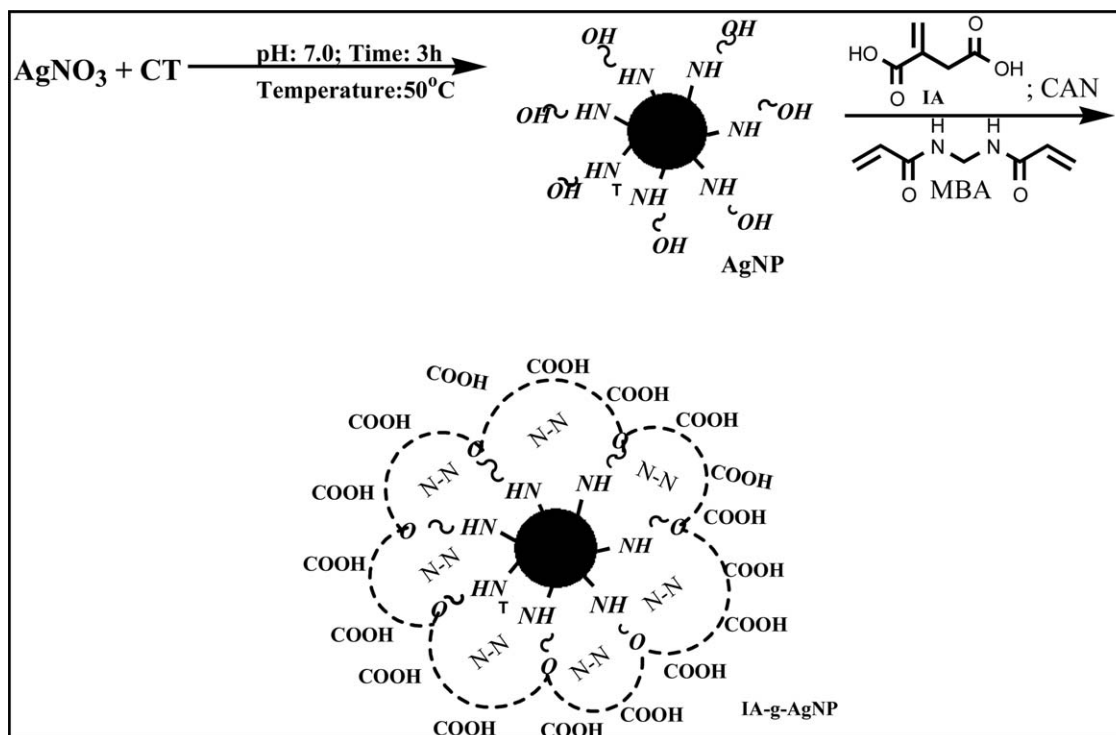
Scheme 1. Predicted mechanism for the synthesis of IA-g-AgNPs.

Statistical Analysis

All of the swelling, release, and antibacterial experiments were carried out in triplicate, and the mean cumulative value (standard deviation) was less than 4.5%. Any data with relative error greater than 4.5% were discarded, and a new experiment was conducted until the error lay within the desired range.

RESULTS AND DISCUSSION

Synthesis of IA-g-AgNPs

Optimization of Reaction Conditions. The reduction of $AgNO_3$ is the most common and widely used technique for the synthesis of AgNPs. Various functional groups on polysaccharides take part in the reduction of Ag^+ ions to Ag^0 and stabilize the nanoparticles. UV–visible spectroscopy is the easiest way to investigate the formation and characterize the morphology of AgNPs. The absorption in the range of 350–500 nm is due to the surface plasmon resonance (SPR) of AgNPs. The peaks around 405 nm indicate pseudospherical shapes, 410 nm indicates spherical shapes, and 335 and 560 nm indicate aggregation of AgNPs.[18]

The effect of pH on the synthesis of AgNPs was studied. The UV–visible spectra for reaction solutions of different initial pHs ranging from 4.0 to 10.0 are given in Figure 1(A). The color of the final solution changes from colorless to light yellow as the pH increases. It is found that the absorption bands were greatly affected by the initial pHs, and all solutions show absorption maxima around 400–430 nm. As the pH increases from 4.0 to 7.0, the intensity of the absorption peak increases, and further increase in pH from 8.0 to 10.0 decreases the absorbance. The peak at pH 7.0 is quite sharp and symmetric

compared to the others; this indicates higher yield and uniqueness in the shape of AgNPs. The lower solubility of CT ($pK_a = 6.5$)[43] at alkaline pH results in the lower yield of AgNPs. The electron pairs of nitrogen present on C-2 of CT is easily available for the reduction of Ag^+ ions at pH 7.0. In acidic conditions, this lone pair of electrons becomes protonated and unavailable. Thus, pH 7.0 was taken as the optimum pH for further studies.
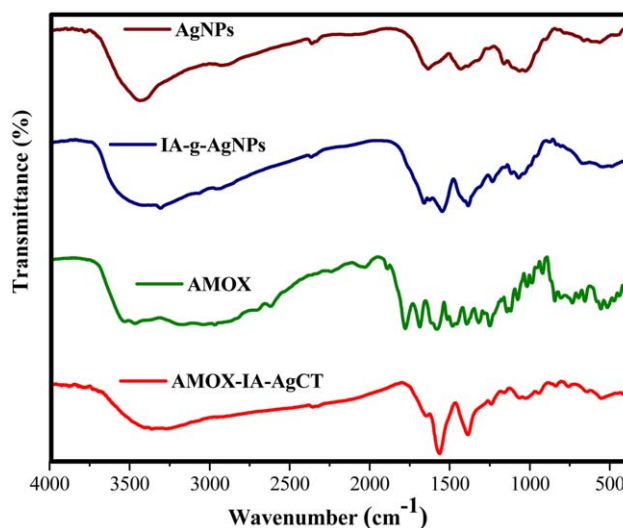

Figure 2. FTIR spectra of AgNPs, IA-g-AgNPs, AMO, and AMO-IA-g-AgNPs. [Color figure can be viewed in the online issue, which is available at wileyonlinelibrary.com.]
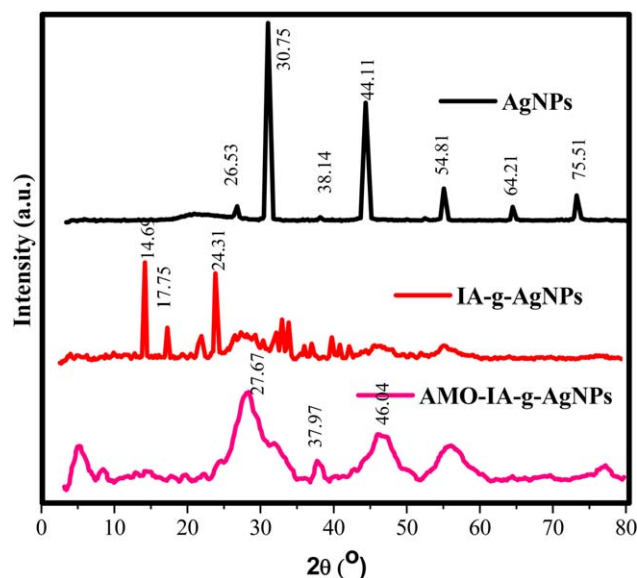
Figure 3. XRD spectra of AgNPs, IA-g-AgNPs, and AMO-IA-g-AgNPs. [Color figure can be viewed in the online issue, which is available at wileyonlinelibrary.com.]

The effect of CT concentration on the synthesis of AgNPs was studied by varying the concentration from 0.1 to 0.6% at pH 7.0. The absorption spectra show symmetric peaks for all concentrations tested [Figure 1(B)]. The maximum absorbance was observed for CT concentrations of 0.2 and 0.3%. The higher concentration of CT (>0.3%) shows lower yield, due to the formation of a viscous solution or lower solubility of CT, so we prefer 0.2% CT as the optimum concentration for the present study.

The synthesis of AgNPs was conducted by using different $AgNO_3$ concentrations ranging from 1.0 to 5.0 mM with 0.2% CT at pH 7.0; this is shown in Figure 1(C). The yield of AgNPs was found to rise with the increase in concentration from 1.0 to 3.0 mM because of the enhanced availability of Ag^+ ions for the reduction, and the peaks corresponding to these concentrations are highly symmetrical. The reaction carried out at higher $AgNO_3$ concentration gives lower yield and shows peaks with absorption maxima in the higher wavelength region. This result confirms the formation of large-sized particles by the adsorption of Ag^+ on the surface of nuclei.[44] Thus, 3.0 mM is
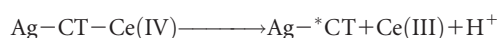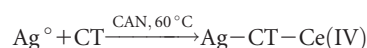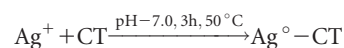
preferred as the optimum concentration of $AgNO_3$ for synthesis of AgNPs.

Figure 1(D) represents the UV–visible spectra of the reactions (3.0 mM $AgNO_3$, 0.2% CT, pH 7.0, incubated for 4 h) carried out at different temperatures (25–55 °C). The solution taken from the reaction medium kept at 25 °C shows no characteristic peak of AgNPs. This result indicates that, at this temperature, 4 h of incubation time is insufficient for the formation of AgNPs. As the reaction temperature increases, the rate of reduction increases and results in higher absorbance in the UV–visible spectra. However, the peak corresponding to an incubation temperature of 55 °C shows a bathochromic shift, due to the enhanced crystal growth around the nucleus,[45] so we chose 50 °C as the optimum temperature.

Figure 1(E) shows the effect of time (30 min to 5 h) on the reaction conducted at optimum temperature, pH, CT and $AgNO_3$ concentration. Time is an important factor that affects the stability and size of AgNPs. From the graph it is found that the intensity of the peak increases with time, and the maximum yield was obtained within 3 h. A further increase in reaction time does not cause any change in absorbance. The probability for the formation of aggregated nanoparticles increases with the increase in time. This confirms that the complete conversion of nanoparticles from ions takes place within 3 h.

Briefly, the optimum conditions for the synthesis of AgNPs are [CT] = 0.2%, [$AgNO_3$] = 3.0 mM, pH = 7.0, temperature = 50 °C, and time = 3 h.

Synthesis of IA-g-AgNPs. AgNPs were well dispersed in distilled water by sonication. The initiator added to the solution decomposes to Ce(IV) ion and makes a complex with CT on the surface of the AgNPs. On further heating, this complex changes to AgNP macroradical with the release of the proton and Ce(III) ion. These reaction steps can be represented as follows:

$$Ag^+ + CT \xrightarrow{pH-7.0,\,3h,\,50\,°C} Ag^\circ - CT$$

$$Ag^\circ + CT \xrightarrow{CAN,\,60\,°C} Ag - CT - Ce(IV)$$

$$Ag - CT - Ce(IV) \xrightarrow{\hspace{2cm}} Ag -\!^*CT + Ce(III) + H^+$$

AgNPs macroradicals were added to the double bond of IA, and a covalent bond is formed between AgNPs and IA. An
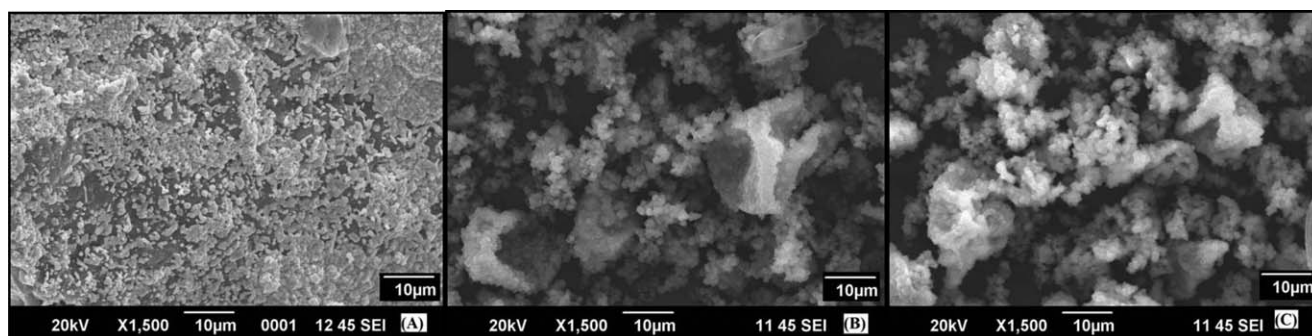

Figure 4. SEM images of (A) AgNPs, (B) IA-g-AgNPs, and (C) AMO-IA-g-AgNPs.
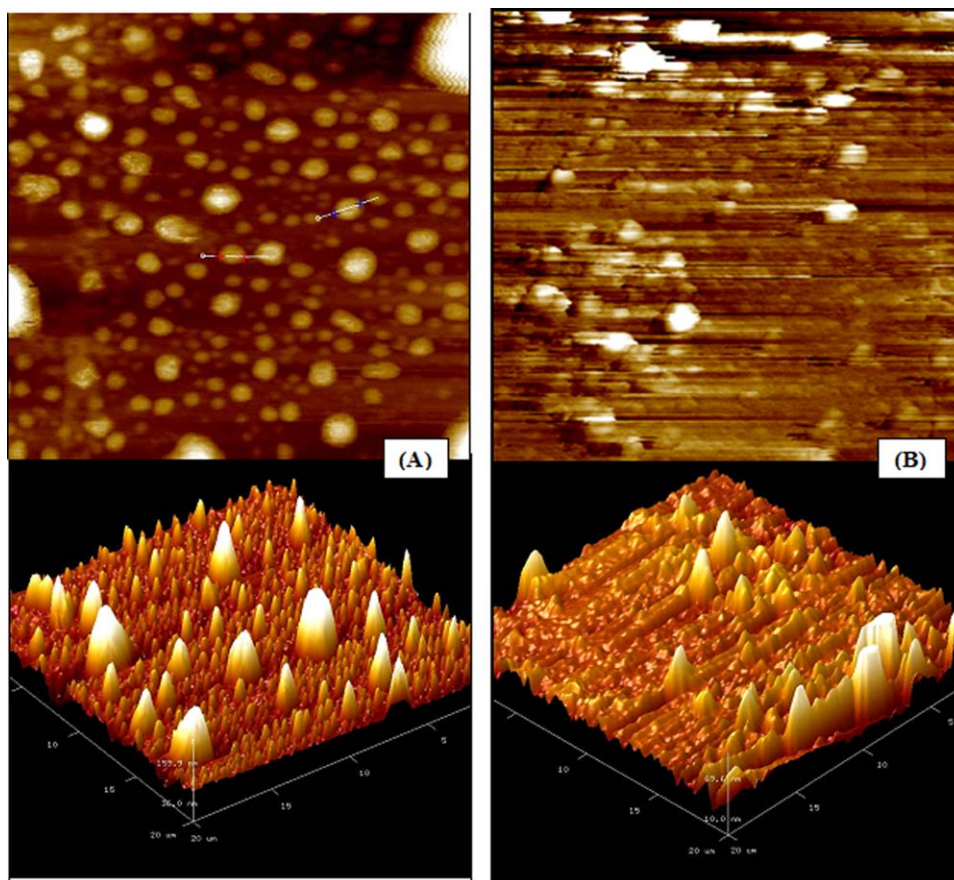
Figure 5. Two- and three-dimensional AFM images of (A) AgNPs and (B) IA-g-AgNPs. [Color figure can be viewed in the online issue, which is available at wileyonlinelibrary.com.]

interpenetrating three-dimensional polymer network with free —COOH groups is formed in the presence of crosslinker (Scheme 1). The surface coating of AgNPs using the hydrogel ensures complete protection and prevents further oxidation of the nanoparticles.

The amount of free carboxyl group in IA-g-AgNPs was found to be 1.67 meq g^{-1}. The DL (%) and EE (%) for AMO onto IA-g-AgNPs were found to be 45.67 and 89.04%, respectively.

Characterization

The FTIR spectra of AgNPs, IA-g-AgNPs, AMO, and AMO-IA-g-AgNPs are given in Figure 2. The FTIR spectrum of AgNPs shows stretching vibrations of N—H (3428 cm^{-1}), O—H (2925 cm^{-1}), N—O (1633 cm^{-1}), and C—N (1160 cm^{-1}), along with the N—H bending vibration present at 1431 cm^{-1}. This result confirms the presence of CT molecules on the surface of AgNPs. Pure CT has the characteristic peaks of —CONH$_2$ at 1657 and 1600 cm^{-1}. In the spectrum of AgNPs, these peaks disappeared, and a new peak appeared around 1635 cm^{-1}. This confirms that the nitrogen atom of CT gets attached to the surface of silver. In the spectrum of IA-g-AgNPs, the peak around 3400 cm^{-1} remains intact with decreased intensity, but a new sharp peak appears at 3307 cm^{-1}, indicating that the secondary —OH group of CT was used for modification. The grafting of IA and MBA was confirmed by the presence of peaks at 1233

(COOH group) and 1546 cm^{-1} (N—H group), respectively. The IR spectrum of AMO shows peaks at 3466 cm^{-1} (—NH$_2$ stretching), 1686 cm^{-1} (O—H stretching), 1393 cm^{-1} (symmetric deformation of —CH$_3$ group), 1249 cm^{-1}, 1075 cm^{-1}, and 555 cm^{-1} (—SO$_3$H group). These data show that the drug used in the present study is pure. The FTIR spectrum of AMO-IA-g-AgNPs is a combination IA-g-AgNPs and AMO. The peak characteristic of —NH$_2$, —OH, —SO$_3$H, and —COOH groups present on the drug and carrier shows a small shift to the shorter wavelength region compared to the pure sample. This suggests that hydrogen bonding or weak van der Waals forces of interactions take place between these functional groups. The peaks around 1600 and 1400 cm^{-1} appear sharper because of the presence of more AMO molecule in the drug carrier. Thus the FTIR spectra confirm the proper loading of AMO onto IA-g-AgNPs.

The XRD patterns of AgNPs, IA-g-AgNPs, and AMO- IA-g-AgNPs are given in Figure 3. The XRD peak confirms the crystalline nature of CT-stabilized AgNPs. A broad hump was observed at 20° due to the amorphous nature of CT. The diffraction peaks in the diffractogram of AgNPs were obtained at $2\theta = 30.75°$, 38.14°, 44.11°, 64.21°, and 75.51°. These peaks are assigned to the Braggs reflections of the (111), (200), (220), (222), and (311) planes of the Face centered cubic (FCC) structure of AgNPs. The high intensity of the (111) peak compared
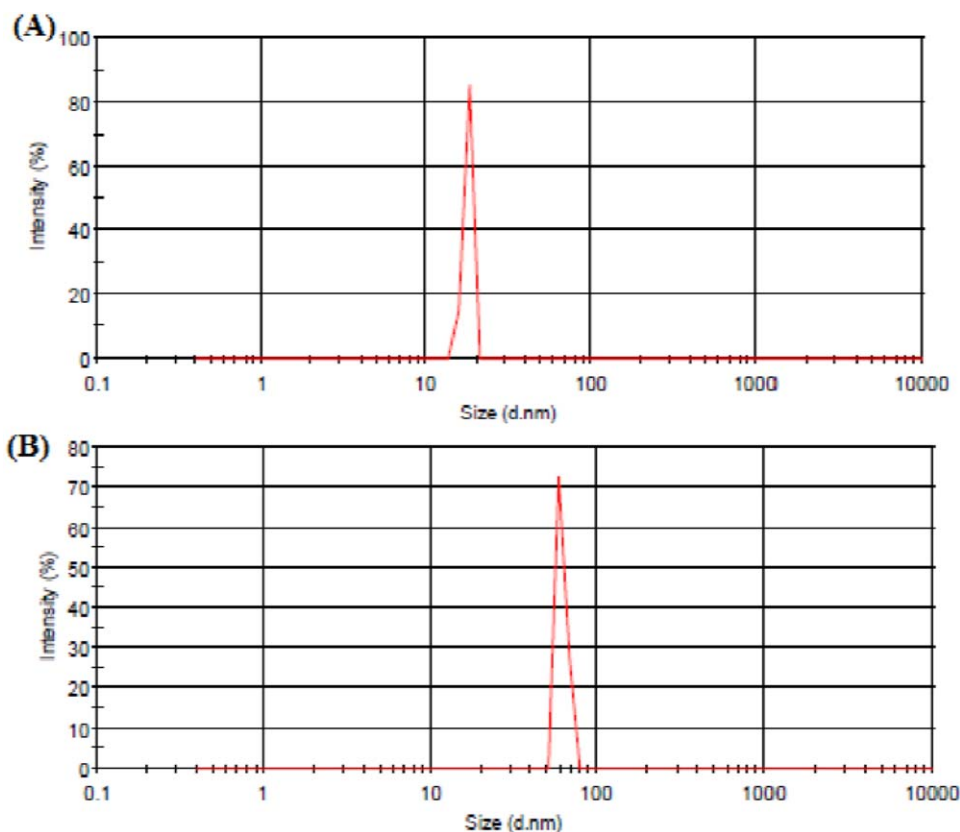
Figure 6. Particle size analysis of (A) AgNPs and (B) IA-g-AgNPs. [Color figure can be viewed in the online issue, which is available at wileyonlinelibrary.com.]

to that of the others indicate that the synthesized AgNPs was mainly composed of the (111) lattice plane.[23,25,26] Previous reports point out that the high intensity of the (111) plane is due to its lower surface free energy compared to the others.[18] An unidentified peak around 54.8°, obtained by the crystallization of the reducing and stabilizing agent used in the synthesis, was also observed in the XRD pattern of AgNPs along with its characteristic peaks. Some reports, used dextran and pullulan as the stabilizing and reducing agents, also get the same result.[46,47]

The crystalline size of synthesized AgNPs was estimated using the Debye-Scherer formula:

$$D = \frac{0.859\ \lambda}{\beta \cos\theta} \qquad (8)$$

where D is the average crystalline size, λ is the wavelength of X-rays (1.5406 Å), β is the full width at half maximum, and θ is the diffraction angle. The above equation is valid only for particles with sizes less than 100 nm.[48] The particle size of AgNPs was found to be about 34.59 nm.

The XRD pattern of IA-g-AgNPs shows weakly crystalline and amorphous peaks characteristic of AgNPs with lower intensity. This confirms the proper modification of CT-stabilized AgNPs by the random grafting of IA in the presence of crosslinker, which decreases the regular arrangement of AgNPs. The X-ray diffractogram of AMO-IA-g-AgNPs has new peaks with increased

basal spacing. Drug loading completely destroys the crystalline nature of the carrier. The increased amorphous nature and basal spacing of the AMO-loaded drug carrier compared to IA-g-AgNPs indicate the greater randomness on the surface. This confirms the proper loading of AMO onto IA-g-AgNPs. The degree of crystallinity among the synthesized samples follows the order AMO-IA-g-AgNPs < IA-g-AgNPs < AgNPs.

SEM analysis was used to study the morphological change in each synthesis stage, and SEM images are given in Figure 4. The AgNPs have a pseudospherical shape with uniform distribution and have particle sizes in the nanometer range. After grafting with IA onto AgNPs, the particle size increases. This morphological change confirms the proper modification of AgNPs. AMO-IA-g-AgNPs has the same morphology as IA-g-AgNPs, which indicates the structural stability of the drug carrier.

The AFM images of AgNPs and IA-g-AgNPs are given in Figure 5. The two-dimensional AFM images confirm the spherical shape of AgNPs with uniform particle size distribution, and that of IA-g-AgNPs shows the particle size ranging from 75 to 80 nm. The three-dimensional AFM image confirms the difference in surface morphology of each stage. The roughness of surfaces can be expressed by two parameters: Ra (average roughness) and RMS (root mean square roughness). The Ra and RMS values for AgNPs were found to be 18.48 nm and 16.71 nm, respectively. After grafting with IA, the values of Ra
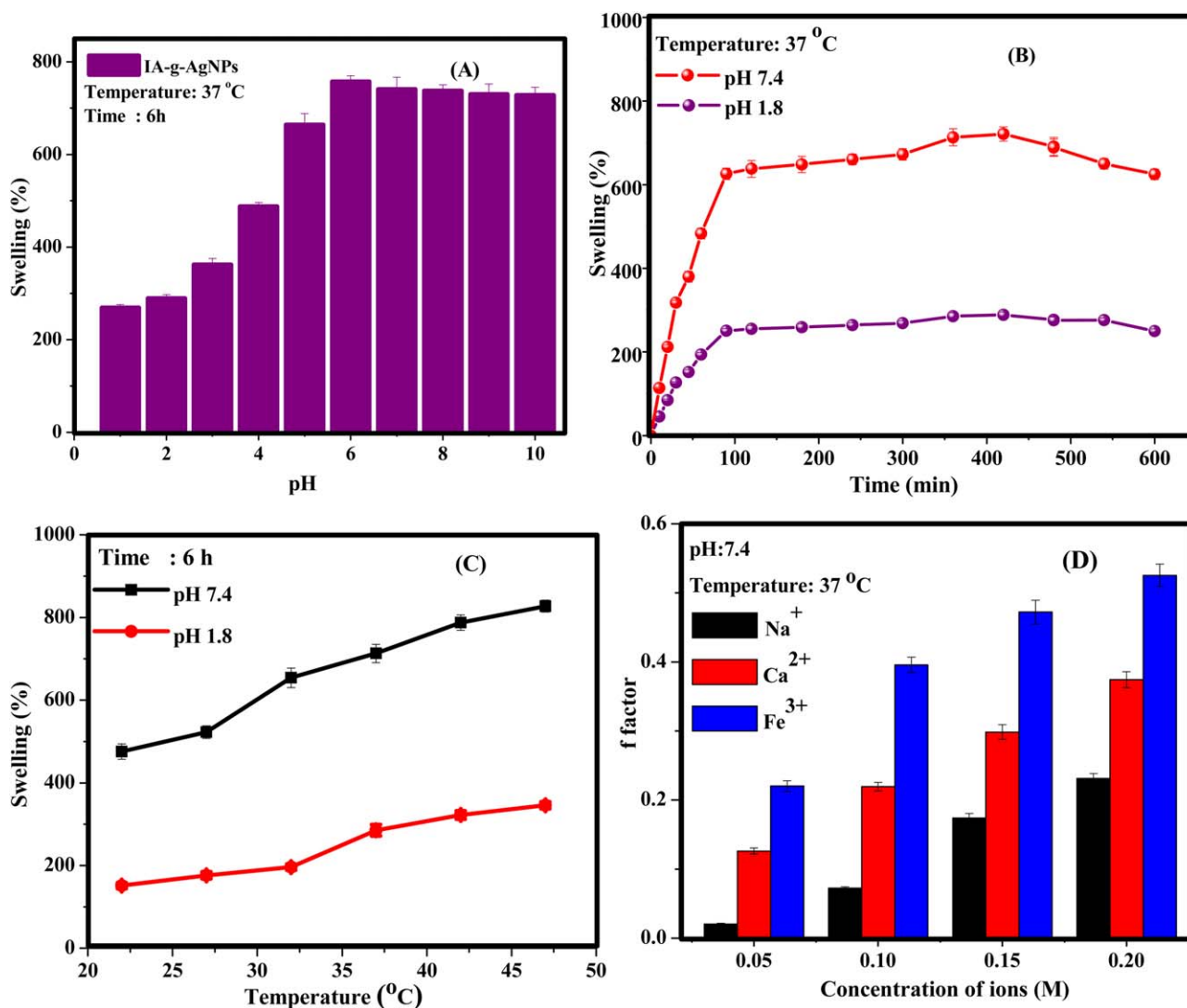
Figure 7. Swelling (%) of IA-g-AgNPs as a function of (A) solution pH, (B) time at two physiological pHs, (C) temperature, and (D) swelling factor in NaCl, $CaCl_2$, and $FeCl_3$ solutions at different concentrations (each point represents the mean value of three samples, and error bars show standard deviation). [Color figure can be viewed in the online issue, which is available at wileyonlinelibrary.com.]

and RMS decrease to 6.07 nm and 5.17 nm, respectively. The decreased roughness confirms that IA-g-AgNPs becomes more amorphous than AgNPs.[49]

The particle size distributions of AgNPs and IA-g-AgNPs were analyzed by the DLS technique (Figure 6). AgNPs has an average size of 20 nm, while IA-g-AgNPs has an average size of 65 nm. The zeta potential values for AgNPs and IA-g-AgNPs were found to be +38.5 and −48.6 mV, respectively. These values confirm the stability and formation of both compounds. Polymer-stabilized AgNPs show a negative charge stabilization.

Swelling Characteristics. The swelling of hydrogels has a great effect on the rate of drug release. The diffusion-controlled drug release increases with an increase in the swelling of the hydrogel. Earlier reports describe the significance of swelling studies on polyionic complexes for the release of AMO.[50] Therefore we conducted swelling studies at different physiological conditions for the synthesized drug carrier.

The pH-sensitive swelling behavior of IA-g-AgNPs was studied at different pHs, and the results are given in Figure 7(A). The swelling percentage was found to increase with an increase in pH and reaches a maximum at 6.0 ($\sim$750 $\pm$ 13.25%). A further increase in pH shows a decrease in swelling. The final drug carrier contains IA, a multi-carboxylate monomer with pK_a values of 3.85 and 5.40. At pH values less than pK_a, most of the —COOH groups are protonated, and enhanced physical cross-linking by hydrogen bonding interaction between functional groups results in complexation. Thus, there is decreased anion–anion repulsion, resulting in a lower swelling percentage in the acidic pH range. At pH values above pK_a, all of the carboxylate groups are ionized and enhance the electrostatic repulsion between ions. Increase anionic density increases the hydrophilicity of the polymer, and it absorbs more water. The lower
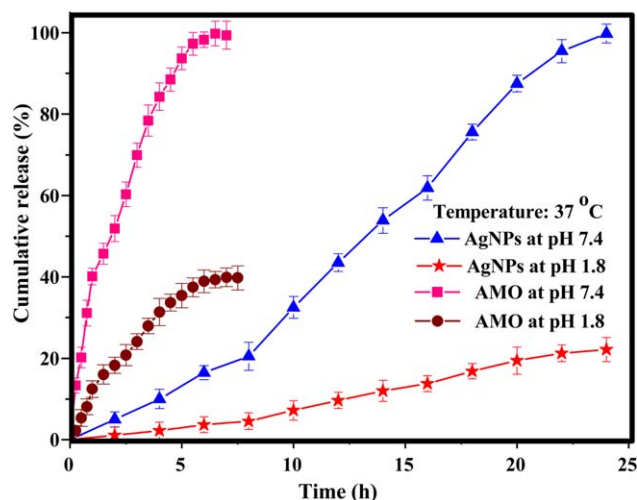
Figure 8. Cumulative release profile of AMO and AgNPs from IA-g-AgNPs at pH 1.8 and 7.4 (each point represents the mean value of three samples, and error bars show standard deviation). [Color figure can be viewed in the online issue, which is available at wileyonlinelibrary.com.]

swelling percentage in a highly basic solution is due to the presence of excess Na^+ ions, which shields the anions and decreases the repulsion.

Figure 7(B) represents the time-dependent swelling behavior of IA-g-AgNPs at physiological pHs (7.4 and 1.8). From the graph it is clear that the swelling of IA-g-AgNPs increases with time. A sharp increase in the initial state is due to the availability of a large number of sites for water absorption. The swelling (%) obtained at pH 1.8 and 7.4 was $288.5 \pm 6.72\%$ and $721.25 \pm 16.80\%$, respectively. IA-g-AgNPs has greater swelling at pH 7.4 compared to 1.8. The ionization of the carboxylate group present on the surface of the drug carrier is greater at alkaline pHs. The enhanced repulsion between these ions and the presence of hydrophilic groups cause a large increase in swelling at pH 7.4. After 8 h, the swelling (%) shows a decrease that may be due to the degradation of polymer at physiological pHs.

The effect of temperature on the swelling behavior of IA-g-AgNPs was studied at different temperatures ranging from 22 to 42 °C. Figure 7(C) shows that the swelling (%) of IA-g-AgNPs at both physiological pHs increases with an increase in temperature. This positive swelling character of IA-g-AgNPs with temperature indicates the occurrence of upper critical solution temperature behavior (UCST).

The effect of ions on the water absorbency behavior of IA-g-AgNPs was studied and is represented in Figure 7(D). A lower swelling (%) was observed in the presence of electrolytes. The effect of cation on the swelling of hydrogel can be found from the value of the swelling factor, *f*. The smaller *f* value for a salt solution compared to an aqueous solution indicates the less salt-sensitive swelling nature of the hydrogel.[51] The *f* value follows the order $Na^+ > Ca^{2+} > Fe^{3+}$. This indicates that Fe^{3+} ions have a greater effect on swelling of IA-g-AgNPs. Swelling (%) was found to decrease with an increase in the charge of metal cation. The multivalent cations coordinate with the

ionized carboxylate ions present on IA-g-AgNPs and act as crosslinkers. This reduces the repulsion between the anions and the network space, which in turn results in lower swelling.

The *f* value also increases with an increase in salt concentration. This indicates that the swelling of IA-g-AgNPs decreases with an increase in salt concentration. The lower swelling (%) of anionic hydrogels with an increase in electrolyte concentration is attributed to the charge-screening effect of cations. As the concentration of electrolyte increases, the water molecules inside the hydrogel are removed by exosmosis. The hydrogel deswells or shows a decrease in swelling (%) or increase *f* value.

***In Vitro* Release and Release Kinetics.** The drug-release profile of AMO and AgNPs from IA-g-AgNPs was studied at simulated intestinal and gastric pHs. The concentrations of AMO and AgNPs were estimated with a UV–visible spectrometer ($\lambda_{max} = 230$ nm) and AAS, respectively. AAS was very much effective in determining very low concentrations of silver. The plots of cumulative release (%) versus time at two pHs for
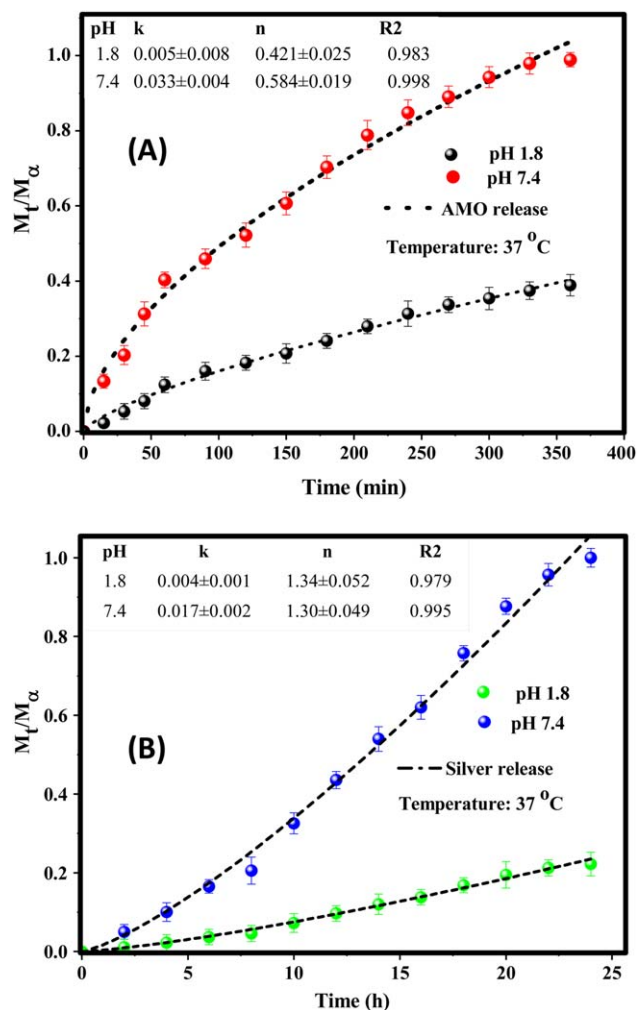

Figure 9. Release kinetics of (A) AMO and (B) AgNPs from IA-g-AgNPs at pH 1.8 and 7.4 (each point represents the mean value of three samples, and error bars show standard deviation). [Color figure can be viewed in the online issue, which is available at wileyonlinelibrary.com.]
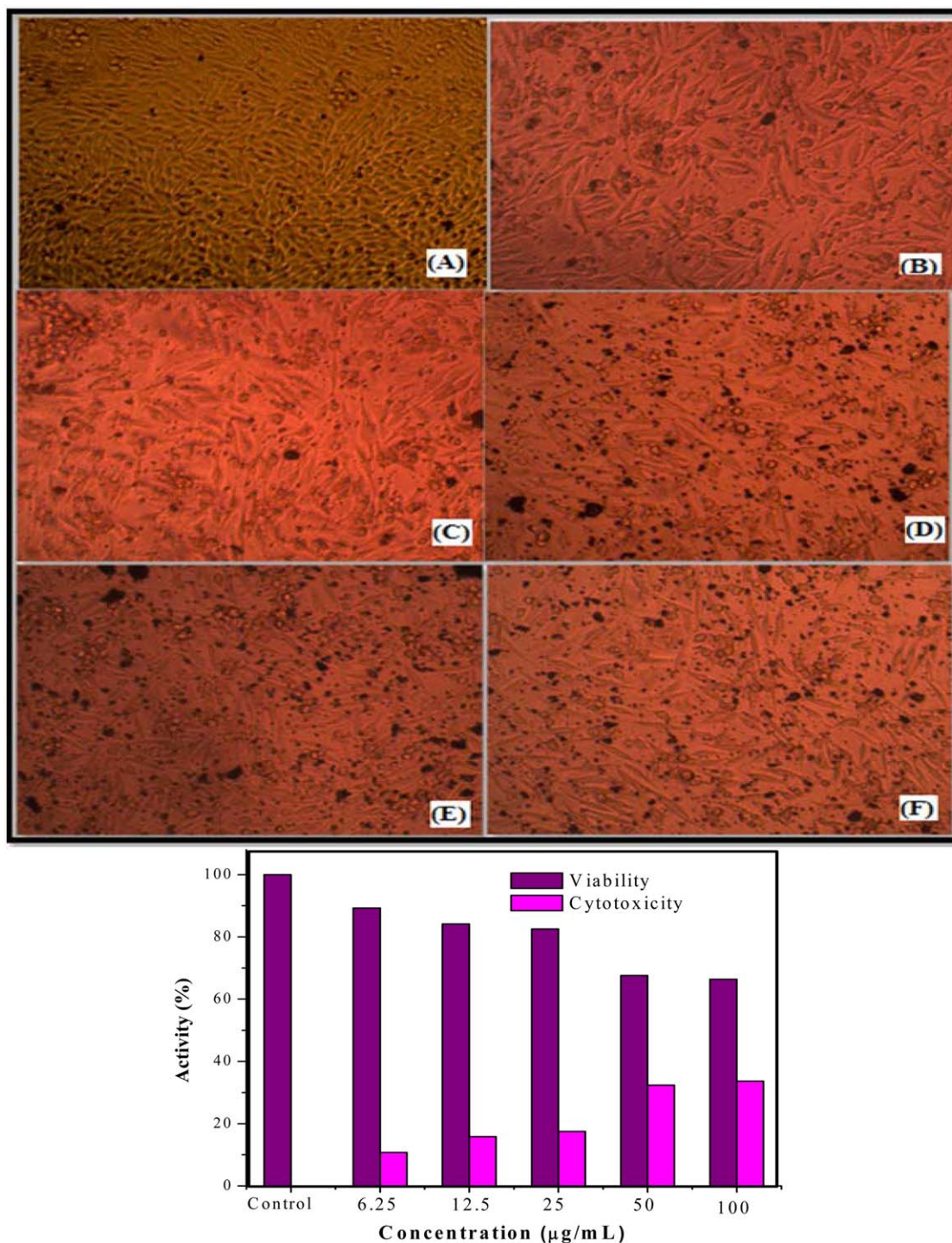
Figure 10. *In vitro* cytotoxicity of IA-g-AgNPs on L929 cells after 24 h. Morphological image of L929 cells with (A) control, (B) 6.25 µg mL^{-1}, (C) 12.5 µg mL^{-1}, (D) 25 µg mL^{-1}, (E) 50 µg mL^{-1}, and (F) 100 µg mL^{-1}. [Color figure can be viewed in the online issue, which is available at wileyonlinelibrary.com.]

AMO and AgNPs are given in Figure 8 and found to be highly pH sensitive. AMO gives more than 90.0% release at pH 7.4, while 35.0% release was observed at pH 1.8 after 6 h. Continuous and sustained release of AgNPs was observed from IA-g-AgNPs after 8 h. Smaller-sized nanoparticles show rapid release kinetics because of their higher diffusivity.

The drug-release kinetics for AMO and AgNPs from IA-g-AgNPs were analyzed by fitting the release data with the Peppas equation (Figure 9). The n value obtained was used to explain the mechanism of drug release: $n = 0.5$ indicates a quasi-Fickian diffusion mechanism, $n > 0.5$ indicates an anomalous non-Fickian drug diffusion, $0.43 < n < 0.855$ indicates both diffusion
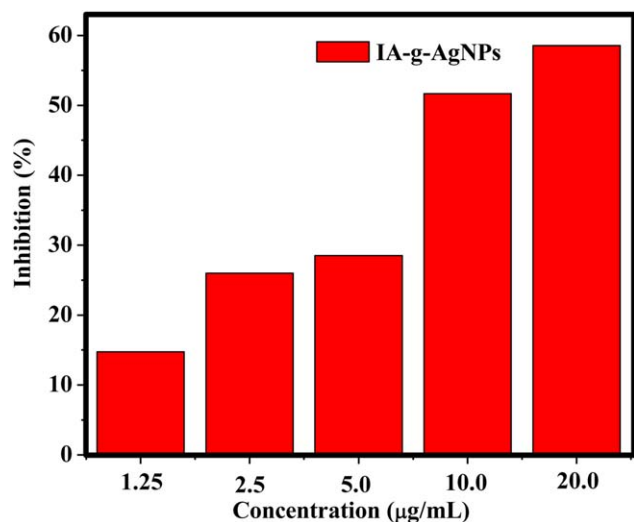
Figure 11. DPPH scavenging activity of IA-g-AgNPs. [Color figure can be viewed in the online issue, which is available at wileyonlinelibrary.com.]

Table I. Zone of Inhibition for AMO-IA-g-AgNPs against *E. coli* and *Staphylococcus*

Sample concentration (μg/mL)	Zone of inhibition (mm)	
	E. coli	*S. aureus*
3.12	0.0 ± 0.000	0.0 ± 0.000
6.25	0.0 ± 0.000	0.0 ± 0.000
12.50	1.2 ± 0.054	1.3 ± 0.057
25.00	1.3 ± 0.036	1.5 ± 0.020
50.00	1.3 ± 0.019	1.6 ± 0.023

and swelling-controlled drug release, and $n > 0.85$ indicates swelling-controlled drug release and polymer relaxation.[16]

The n values were 0.584 ± 0.019 and 0.421 ± 0.025 at pH 7.4 and 1.8, respectively, for AMO. The release of AMO at alkaline pH is controlled by diffusion of the drug followed by swelling of the polymer. A smaller k value indicates mild interaction between drug and drug carrier. From the Figure 9 it is clear that AMO shows a three-step release. First the drug attached to the surface of the carrier is released, then the polymer swells, which enhances the release of water-soluble drugs, and the final step is the degradation of polymer. A diffusion-controlled release of AMO was observed at acidic pH.

The n value obtained for AgNPs release from the kinetic model is >0.85 at pH 7.4. This confirms that the release of AgNPs

from IA-g-AgNPs is controlled by swelling or polymer relaxation. The swelling of the drug carrier took place for the first 8 h. The amount of AgNPs released for the first 8 h is $20.5 \pm 3.45\%$ and $4.4 \pm 2.05\%$ at pH 7.4 and 1.8, respectively. After 8 h, a rapid and sustained release of AgNPs was observed, due to the complete degradation of hydrogel and CT coating. Thus, the release of AgNPs is controlled by degradation of the polymer more than by the swelling. The low release of AgNPs at acidic pH may be due to the low degradation rate of IA-g-AgNPs. *In vitro* release data confirm that IA-g-AgNPs is suitable for the delivery of AMO and AgNPs in a basic environment.

Evaluation of Cytotoxicity on L929 Cells. The cytotoxicity of IA-g-AgNPs was evaluated by MTT assay on L929 cell lines, and the results are shown graphically in Figure 10. IA-g-AgNPs shows dose-dependent cytotoxicity after 24 h incubation. Approximately 90.0% and 70.0% viability was found for 6.25 and 100.0 μg/mL of IA-g-AgNPs, respectively. The prepared sample shows greater than 50.0% viable cells for all concentrations tested. This indicates that IA-g-AgNPs has no significant toxicity and assures that the present material is a safe drug carrier.
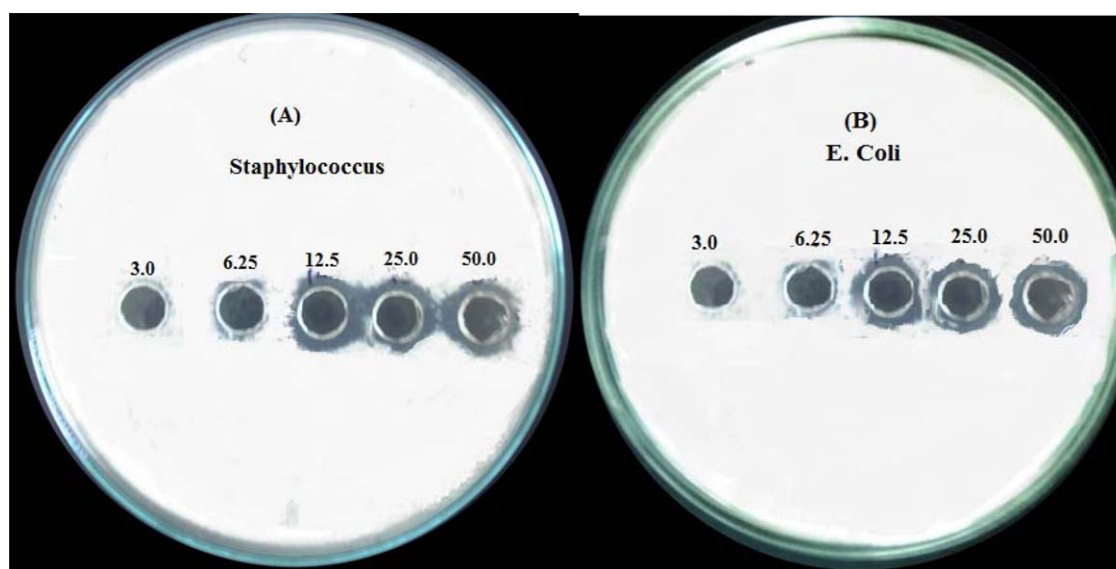

Figure 12. Inhibition zones of AMO-IA-g-AgNPs against (A) *Staphylococcus* and (B) *E. coli*. [Color figure can be viewed in the online issue, which is available at wileyonlinelibrary.com.]

Antioxidant/DPPH Assay. The amount of DPPH radical formed was compared with that of ascorbic acid. The inhibition was found to be increased with an increase in concentration of IA-g-AgNPs (Figure 11). The 10.0 μg/mL of IA-g-AgNPs shows more than 50.0% inhibition percentage. This lower IC_{50} value confirms that the synthesized IA-g-AgNPs has excellent free-radical scavenger properties and can act as an effective primary antioxidant.

Antibacterial Assay of AMO-IA-g-AgNPs. *In vitro* profiling of the antibacterial activity of AMO-IA-g-AgNPs was studied using five different concentrations ranging from 3.0 to 50.0 μg/mL. The antibacterial properties were studied against *Escherichia coli* (*E. coli*) (gram-negative bacteria) and *Staphylococcus aureus* (*S. aureus*) (gram-positive bacteria) by plate assay, and the formation of a clear zone was measured. Figure 12 and Table I clearly indicate that AMO-IA-g-AgNPs has antibacterial activity against both gram-positive and gram-negative bacteria. The zone of inhibition was 1.2 ± 0.054 mm and 1.3 ± 0.057 mm for *E. coli* and *S. aureus* at a 12.5 μg/mL concentration of the sample. The inhibition zone in the range 1.0–2.0 mm may be due to the low concentration of AMO-IA-g-AgNPs. Minimum inhibitory concentration (MIC) of IA-g-AgNPs for both *E. coli* and *S. aureus* was found to be 12.5 μg/mL. The susceptibility of *E. coli* and *S. aureus* toward AMO-IA-g-AgNPs may be due to plasmolysis of the cell wall, cytoplasm separation from the bacterial cell wall, or inhibition of bacterial cell wall synthesis.

CONCLUSIONS

The present work deals with the synthesis of IA-g-AgNPs, which can act as a dual antimicrobes to overcome bacterial resistance in presence of AMO. Chitosan acts as a good stabilizing and reducing agent for the synthesis of AgNPs at optimized conditions (pH: 7.0, [CT]: 0.2%, [AgNO$_3$]: 3.0 mM, time: 3 h, temperature: 50 °C). The results of the FTIR, AFM, and SEM analyses confirm the formation of AgNPs, IA-g-AgNPs, and AMO-IA-g-AgNPs. The XRD spectrum confirms the crystallinity and formation of AgNPs. The zeta potential and DLS experiments show that AgNPs are stable and nanometer-sized. The swelling of IA-g-AgNPs was found to be thermo, ionic, and pH responsive. The *in vitro* release of AMO and AgNPs from IA-g-AgNPs was found to be higher at intestinal pH than at gastric pH. The release kinetics data fitted with the Peppas equation show a swelling-controlled three-step release for AMO and degradation-controlled release for AgNPs. *In vitro* cell viability analysis on L929 cell lines confirms the biocompatibility, and a DPPH assay confirms the antioxidant property of IA-g-AgNPs. AMO-IA-g-AgNPs has greater antibacterial efficacy against both gram-positive and gram-negative bacteria. The antioxidant, antimicrobial, and cytotoxic analyses show that silver polymer nanocomposite is an efficient candidate for medical applications as an antibacterial agent.

REFERENCES

1. Shahverdi, A. R.; Fakhimi, A.; Shahverdi, H. R.; Minaian, S. *Nanomedicine* **2007**, *3*, 168.

2. Yu, D. G.; Teng, M. Y.; Chou, W. L.; Yang, M. C. *J. Membrane Sci.* **2003**, *225*, 115.

3. El-Batal, A. I.; Haroun, B. M.; Farrag, A. A.; Baraka, A.; El-Sayyad, G. S. *Br. J. Pharm. Res.* **2014**, *4*, 1341.

4. Li, P.; Li, J.; Wu, C.; Wu, Q.; Li, J. *Nanotechnology* **2005**, *16*, 1912.

5. Souli, M.; Christine, B. W.; George, M. E. *Int. J. Antimicrob. Agents* **1998**, *10*, 23.

6. Fonze, E.; Vanh́ove, M.; Dive, G.; Sauvage, E.; Frere, J. M.; Charlier, P. *Biochemistry* **2002**, *41*, 1877.

7. Buynak, J. D.; Ramana, D. V.; Adam, G. *Bioorg. Med. Chem. Lett.* **2000**, *10*, 853.

8. Jones, R. N.; Marshall, S. A.; Varnam, D. *J. Diagn. Microbiol. Infect. Dis.* **1998**, *32*, 85.

9. Gianluigi, F.; Annarita, F.; Stefania, G.; Luciana, P.; Mahendra, R.; Giancarlo, M.; Massimiliano, G. *Molecules* **2015**, *20*, 8856.

10. Dhrutika, P.; Miral, P.; Krishnamurthy, R. *CIBTech J. Bio-Protoc.* **2013**, *2*, 50.

11. Huang, N. M.; Radiman, S.; Lim, H. N.; Khiew, P. S.; Chiu, W. S.; Lee, K. H.; Syahida, A.; Hashim, R.; Chia, C. H. *Chem. Eng. J.* **2009**, *155*, 499.

12. Thierry, D.; Paola, N.; Douglas, G.; Giacomo, C.; Cesar, P.; Barbara, D. B.; Frederic, G.; François, R. *Colloids Surf., A* **2012**, *395*, 145.

13. Yen-Chi, H.; Yu-Min, C.; Wei-Li, L.; Yi-Fen, L.; Ying-Nan, C.; Jiang-Jen, L. *J. Colloid Interface Sci.* **2010**, *352*, 81.

14. Mohan, Y. M.; Vimala, K.; Thomas, V.; Varaprasad, K.; Sreedhar, B.; Bajpai, S. K.; Raju, K. M. *J. Colloid Interface Sci.* **2010**, *342*, 73.

15. da Costa, L. P.; Formiga, A. L. B.; Mazali, I. O.; Sigoli, F. A. *Synth. Met.* **2011**, *161*, 1517.

16. Isabel, P. S.; Luis, M. L. M. *Adv. Funct. Mater.* **2009**, *19*, 679.

17. Clemens, B.; Xiaobo, C.; Radha, N.; Mostafa, A. E. *Chem. Rev.* **2005**, *105*, 1025.

18. Andrade, P. F.; Faria, A. F.; Silva, D. S.; Bonacin, J. A.; Goncalves, M. d. C. *Colloids Surf., B* **2014**, *118*, 289.

19. Vasileva, P.; Donkova, B.; Karadjova, J.; Dushkin, C. *Colloids Surf., A.* **2011**, *382*, 203.

20. Ravindran, A.; Chandran, P.; Khan, S. S. *Colloids Surf., B* **2013**, *105*, 342.

21. Kendra, D. F.; Hadwiger, L. A. *Exp. Mycol.* **1984**, *8*, 276.

22. Sudarshan, N. R.; Hoover, D. G.; Knorr, D. *Food Biotechnol.* **1992**, *6*, 257.

23. Tsai, G. J.; Su, W.-H. *Food Protect.* **1999**, *62*, 239.

24. Vimala, K.; Mohan, Y. M.; Varaprasad, K.; Red, N. N.; Ravindra, S.; Naidu, N. S.; Raju, K. M. *J. Biomater. Nanobiotechnol.* **2011**, *2*, 55.

25. Qi, L.; Xu, Z.; Jiang, X.; Hu, C.; Zou, X. *Carbohydr. Res.* **2004**, *339*, 2693.

26. Mirzaei, E. B.; Ramazani, S. A.; Shefiee, M.; Danaei, M. *Int. J. Polym. Mater. Polym. Biomater.* **2013**, *62*, 605.

27. Sadrolhosseini, A. R.; Noor, A. S. M.; Moksin, M.; Abdi, M. M.; Mohammadi, A. *Int. J. Polym. Mater. Polym. Biomater.* **2013**, *62*, 284.

28. Yu, Y.; Jia, F.; Li, S.; Yan, S.; Ling, C.; Yuan, K. *Int. J. Polym. Mater. Polym. Biomater.* **2013**, *62*, 450.

29. Anirudhan, T. S.; Parvathy, J. *Des. Monomers Polym.* **2015**, *18*, 413.

30. Anirudhan, T. S.; Parvathy, J. *Polym. Plast. Technol. Eng.* **2014**, *53*, 1339.

31. Giri, T. K.; Thakur, A.; Alexander, A.; Ajazuddin; Badwaik, H.; Tripathi, D. K. *Acta Pharm. Sin. B* **2012**, *2*, 439.

32. Ali, H.; Hashem, M.; El-Hady, M. M. A.; Sharaf, S. *Carbohydr. Polym.* **2013**, *92*, 407.

33. Song, J.; Kang, H.; Lee, C.; Hwang, S. H.; Jang, J. *ACS Appl. Mater. Interfaces* **2012**, *4*, 460.

34. Yook, J. Y.; Choi, G.; Suh, D. H. *Chem. Commun.* **2012**, *48*, 5001.

35. Ahmed, M. Y.; Hussein, A. Y.; Samah, M. E.; Samir, K. *Int. J. Biol. Macromol.* **2015**, *76*, 25.

36. Mehdi, Y.; Sana, F.; Hassan, N. *Int. J. Biol. Macromol.* **2015**, *79*, 37.

37. Jing, A.; Qingzhi, L.; Xiaoyan, Y.; Desong, W.; Xueyan, L. *J. Appl. Polym. Sci.* **2011**, *120*, 3180

38. Anirudhan, T. S.; Rejeena, S. R. *J. Appl. Polym. Sci.* **2014**, *2014*, 40699.

39. Sudha, C.; Angadi, L. S.; Manjeshwar, T. M.; Aminabhavi, *Int. J. Biol. Macromol.* **2012**, *51*, 45.

40. Xiong, M.; Bao, Y.; Yang, X.; Zhu, Y.; Wang, J. *Adv. Drug Deliv. Rev.* **2014**, *78*, 63.

41. Singh, B.; Sharma, V. *Carbohydr. Polym.* **2014**, *101*, 928.

42. Salem, H. F.; Eid, K. A. M.; Sharaf, M. A. *Int. J. Drug Deliv.* **2011**, *3*, 293.

43. Riva, R.; Ragelle, H.; Rieux, A.; Duhem, N.; Jerome, C.; Preat, V. *Adv. Polym. Sci.* **2011**, *244*, 19.

44. Yang, N.; Li, W. *Ind. Crops Prod.* **2013**, *48*, 81.

45. Mittal, A. K.; Bhaumik, J.; Kumar, S.; Banerjee, U. C. *J. Colloid Interface Sci.* **2014**, *415*, 39.

46. Kanmani, P.; Lim, S. T. *Carbohydr. Polym.* **2013**, *97*, 421.

47. Bankura, K. P.; Maity, D.; Mollick, M. M. R.; Mondal, D.; Bhowmick, B.; Bain, M. K. *Carbohydr. Polym.* **2012**, *89*, 1159.

48. Boulch, F.; Schouler, M. C.; Donnadieu, P.; Chaix, J. M.; Djurado, E. *Image Anal. Stereol.* **2001**, *20*, 157.

49. Ferreira, F. C.; Curvelo, A. A. S.; Mattoso, L. H. C. *J. Appl. Polym. Sci.* **2003**, *89*, 2957.

50. Torre, P. M. D.; Enobakhare, Y.; Torrado, G.; Torrado, S. *Biomaterials* **2003**, *24*, 1499.

51. Anirudhan, T. S.; Binusreejayan; Rejeena, S. R. *Int. J. Polym. Mater.* **2014**, *63*, 539.